RESEARCH ARTICLE

Experimental study on oscillating grid turbulence and free surface fluctuation

Luca Chiapponi · Sandro Longo · Mara Tonelli

Abstract This paper analyses the interaction between the turbulence and free surface. The phenomenon takes place in many natural flows and industrial processes. In the present experiments, turbulence is generated by a vertically oscillating grid moving beneath the free surface. Fluid velocity has been measured through a hot-film anemometer, and the free surface elevation has been measured by an ultrasonic sensor. Integral length scales and several turbulence estimators have been computed. In order to detect the generation of turbulence near the free surface, the correlation between free surface elevation and the underneath flow velocity has been studied, as well as the time lag between turbulence and free surface. The free surface dynamics has been characterized by a velocity scale and a length scale. The kinetic energy associated with the free surface fluctuations increases with the Reynolds number at a rate depending on the frequency of the grid movement. For Reynolds number larger than ≈ 1000, however, the relationships collapse to a single curve characterized by a lower rate. The present experiments do not achieve the inertial sub-range in the vertical velocity fluctuations, and the estimated spectrum decays with an exponent smaller than -3, which is the typical value for the two-dimensional turbulence in the inertial sub-range. The macro length scale, estimated by using the Taylor's frozen turbulence hypothesis, experiences a decay away from the grid, which follows reasonably well the profile of Thompson and Turner (J Fluid Mechanics 67: 349–368, 1975). The micro length scale reduces immediately beneath the free surface, which can be interpreted by the increase of dissipation rate in the subsurface layer. The classification diagram by Brocchini and Peregrine (J Fluid Mech 449: 225–254, 2001) indicates that most tests fall in the weak turbulence domain, but some tests fall in the wavy domain. The vertical velocity fluctuations and the free surface level show a significant correlation with a negative phase lag, that is, the free surface fluctuations are ahead of the vertical velocity fluctuations.

List of the symbols

$\overline{\cdots}$	Time average operator
$\widetilde{\cdots}$	Slowly varying term operator
$\widehat{\cdots}$	Slowly varying term plus fluctuating term operator
$\otimes$	Dyadic product operator
$E\{\ldots\}$	Ensemble average operator
α, α_p	Angle, principal axis of the Reynolds stress tensor angle
κ	Turbulent kinetic energy
Λ	Integral length scale
λ	Taylor length scale
ρ	Water mass density
σ	Surface tension
v	Kinematic fluid viscosity
$\chi_{w'w'}$	Autocorrelation coefficient
τ	Time lag

L. Chiapponi · S. Longo (✉)
Department of Civil Engineering, University of Parma,
DICATeA, Parco Area delle Scienze, 181/A, 43124 Parma, Italy
e-mail: sandro.longo@unipr.it

L. Chiapponi
e-mail: luca.chiapponi@unipr.it

Present Address:
S. Longo
CUED, Cambridge, UK

M. Tonelli
Dipartimento di Chimica, Fisica e Ambiente, DCFA, Università degli Studi di Udine, via del Cotonificio, 108, 33100 Udine, Italy
e-mail: mara.tonelli@uniud.it

Υ	Integral time scale
υ	Taylor time microscale
ψ	Coherence
a, A	Coefficient
DAQ	Data acquisition board
DOA	Degree of anisotropy
d	Water depth
f_G	Frequency of the grid
Fr, Fr_s	Froude number, based on free surface scales
g	Gravity acceleration
H, H_{rms}, H_{max}	Wave height, root mean square wave height, maximum wave height
$H_{1/3}, H_{1/10}$	Highest one-third wave, one-tenth wave, etc.
L	Length scale
L_w, L_∞	Integral length scale in the vertical, far field longitudinal integral length scale
LDV	Laser Doppler velocimetry
M	Mesh size
P_{ab}	Power cross-spectral density between the variables a and b
q	Velocity scale
R	Water depth above the maximum level of the grid
$R_{w'w'}$	Time correlation function for the vertical fluctuating velocities
R^2	Coefficient of determination
Re, Re_G, Re_L, Re_s	Reynolds number, of the grid, based on the grid parameters, based on surface scales
S	Stroke
s	Thickness of the grid bar
t	Time
t_{ave}	Interval time of average
$T_{mean}, T_{1/3},\ldots$	Period of the waves, mean value, mean value of the first third, etc.
TKE	Turbulent kinetic energy
u, w	Horizontal, vertical fluid velocity
u'_{rmsHT}	Hopfinger and Toly (1976) horizontal velocity fluctuation r.m.s. value
u', w'	Horizontal, vertical fluctuating fluid velocity
u'_{rms}, w'_{rms}	Horizontal, vertical fluctuating fluid velocity r.m.s. value
$w'_{rms\infty}$	Far field vertical fluctuating velocity r.m.s. value
u_s	Velocity scale based on interface kinematics
V, V_1, V_2	Velocity
V', V'_1, V'_2	Fluctuating velocity
W	Velocity scale
We_s	Weber number, based on surface scales
z	Vertical spatial coordinate
zt_3	Bed stress log layer limit
z_G	Distance of the mean position of the grid from the still water level
z_s	Instantaneous level of the free surface

1 Introduction

Numerous interface processes are controlled by the structure and local dynamics of turbulence. Examples include gas and heat exchange in oceans (large scale) and chemical reactions in industrial and manufacturing processes (small scale). The interface represents a moving boundary for the water flow and imposes certain conditions: the material derivative of the free surface must be zero, while the tangential stresses should be zero unless a shear is exerted by the overflowing gas. The interaction between internal turbulence and free surface is expected to vary with two important parameters: the Reynolds number and the Froude number based on near interface scales. At small Froude numbers, the free surface is essentially unaffected by the turbulence of the flow beneath, so it is almost flat. In this situation, the interface may be treated as a slip-free rigid flat plate. At large Froude numbers, the free surface is distorted and an energy exchange with the fluid flow takes place. Such an exchange can be either very limited or quite strong. In the latter case, a free surface becomes discontinuous, and air bubbles and drops form. Reynolds number indicates the role of viscosity in the free surface boundary layer, which is only important when the free surface is flat and smooth. There is a great variety of free surface patterns and several mechanisms of energy transfer at a free surface. In natural environments, the most common type of surface deformation is waves in a wide range of length and period, controlled by surface tension and gravity. It is also well known that turbulent bursting at the bottom of channels can reach the free surface, leading to a high level of surface exchange. A general description of various interactions between free surfaces and turbulence is reported in Brocchini and Peregrine (2001), where four regimes of free surface distortion as a consequence of water turbulence are classified, based on the length scale and velocity scale of turbulence. The Froude number and the Weber number based on these scales are introduced, in order to define the relative magnitude of the effects of gravity and surface tension.

A recent paper by Hunt et al. (2011) gives an interpretation and a mathematical description of the role of the viscous layer on both sides of an interface between two layered fluids, assuming that each fluid is in turbulent motion with zero mean flow; this situation fits well with the experimental condition of the present study, even though Hunt et al. model assumes that the interface is flat at all stages. According to their model, if turbulence is forced in the lower fluid, also characterized by a density larger than the upper fluid and if the initial turbulence in the lower fluid is much stronger than in the upper fluid, then viscous action is responsible of driving fluctuations in the upper fluid. This situation is certainly correct in the short term, since Hunt et al. (2011) adopt a rapid distortion model, but holds true also in the long term, when nonlinear effects become significant. The result is that the interfacial velocity fluctuations are of the same order of the homogeneous turbulence in the fluid domain, with some amplification by the blocking effect. The main difference with the present experiments is the distortion of the interface and the development of eddies near the interface, intrinsically included in Brocchini and Peregrine (2001) analysis but not in Hunt et al. (2011) model.

This experimental activity is inserted in a general framework with the aim of a validation of the existing classifications of the turbulence interactions at the interface between two fluids (usually a liquid in the lower side and a gas in the upper side), and specifically the classification by Brocchini and Peregrine (2001). Past experiments in the same framework are shortly recalled. A first series of experiments refer to free surface turbulence generated in the liquid domain by a Crump weir (Longo 2011). In this paper, the turbulence macro length scale is evaluated through the autocorrelation of experimental data and it appears that this scale is generally smaller than the geometric scale of the dominant surface features. In reality, these two scales can be completely unrelated, for example, eddies of weak turbulence are much smaller than the wave length of gravity waves. A second set of experiments refer to the turbulence beneath wind generated waves in a wind tunnel (Longo 2012; Longo et al. 2012a, b; Longo and Losada 2012), where turbulence is forced by the air side, while turbulence on the water side is generated by the flow shear and enhanced by micro-breaking (micro-breaking is a small-scale breaking without air entertainment). The best results (i.e., the best correlation with the visual aspect of the free surface) were obtained by assuming the same length scale for turbulence and free surface waves, where a velocity scale was computed from a weighted average of the turbulence kinetic energy at the free surface, with weights equal to the mass density of water and air. The contribution to the velocity scale by the turbulence on the air side is generally weak due to the low density, but is

conceptually needed in free surface classification when the water is almost at rest. It seems also evident that, in presence of well-developed gravity waves, the dominant length scale at the free surface is slightly correlated with turbulence. Because turbulence does not contain only a single length scale, especially near a boundary, the integral length scale may not be the proper choice.

In this study, the turbulence generator is a vertical oscillating grid in a shear-free surface tank. The flow involves the interactions between jets and wakes due to the periodic motion of the grid bars, but, at sufficient distance from the grid, these coherent structures almost disappear leaving a nearly isotropic and homogeneous turbulence. If the turbulent flow field interacts with a shear-free interface, a boundary layer develops close to the interface, within which no mechanism of turbulence generation exists unless micro-breaking is present. The absence of turbulence generation inside a boundary layer is quite uncommon, and few experiments have been reported in literature.

The theory of turbulence in a homogeneous fluid induced by an oscillating grid is presented in Long (1978) and several experiments in grid-stirred tank are documented. In order to have a nearly isotropic turbulence with zero mean flow, the grid should have a solidity (the ratio of the area occupied by the bars and the total area of the grid) less than 40 %, a frequency less than 7 Hz, and measurements should be taken 2 or 3 mesh sizes away (De Silva and Fernando 1994). Aiming to quantify the spatially decaying of turbulence in the presence of a density interface, due to salinity difference, Hopfinger and Toly (1976) used a 2D LDV in a grid-stirred tank. Aiming to analyze the gas transfer in the air–water interface induced by oscillating grid turbulence, Herlina and Jirka (2008) performed some experiments in a grid-stirred tank using a combined particle image velocimetry and laser-induced fluorescence, with the latter technique used for measuring the dissolved gas concentration field. Thompson and Turner (1975), Dickinson and Long (1978), McDougall (1979), Brumley and Jirka (1987) performed experiments in a grid-stirred tank giving information on the spatial variations of the integral length scale and velocity fluctuations. The present experiments differ from all the other similar experiments because the action of the grid is strong enough to distort significantly the free surface, generating evident free surface fluctuations and waves. Also the statistics of the free surface fluctuations and the correlation with the impinging turbulence are analyzed.

Despite the advantages of a grid-stirred tank with respect to other turbulence generators, several caveats arise as documented in the quoted references and also from ad hoc experiments performed to verify the repeatability of the tests (McKenna and McGillis 2004). McKenna and McGillis (2004) found that the mean flow may vary up to

25 % and turbulent fluctuations may vary up to 15 % from one run to another. In addition, the flow field is sensitive to the initial conditions and disturbances, and secondary flows develop due to the nonlinear effect. In particular if a disturbance in velocity is superimposed to the grid motion in the upward domain, the upward part of the grid motion transfers more energy to the flow than does the down-going part of the oscillation cycle. Hence, any external disturbance can be amplified (McDougall 1979). All these problems can be overcome, as long as certain precautions are adopted in carrying out the experiments and in analyzing the data. Since the experiments cannot completely eliminate the secondary flows, these secondary flows should be considered as a part of the flow instead of a disturbance. Sometimes it is possible to elucidate their effects on turbulence (e.g., Hopfinger and Toly 1976, about their influence on spatial decay of turbulence), but most of their effects are intimately connected to the global flow dynamics and it is difficult to isolate them.

Since grid-stirred tank can show significant flaws, varying in different tanks, a preliminary calibration of this grid-stirred tank is necessary.

The paper is organized as follows. In Sect. 2, the experimental apparatus, the experimental procedure, and the test program are detailed. In Sect. 3, the experimental results are analyzed, including the macrovortices, length scales, the spectral distribution of the turbulent energy, and the correlation between free surface and velocity fluctuations. The conclusions are presented in Sect. 4.

2 Experimental arrangement

2.1 Installation

The experiments were performed in a 570 mm square tank 420 mm deep (Fig. 1), with PVC front, side and back panels. The box was properly fastened to minimize vibration, which will contribute to the generation of surface waves. The grid is a perforated stainless steel sheet, 2 mm thick with the 10 mm square holes spaced at $M = 12$ mm center to center. The solidity, defined as the ratio of the area occupied by the bars and the total area of the grid, is equal to 31 % and is quite similar to that (equal to 36 %) used by Thompson and Turner (1975), Hopfinger and Toly (1976), McDougall (1979), Brumley and Jirka (1987), but the mesh size is about five times smaller. The walls of the tank are planes of symmetry with respect to the mesh pattern to minimize secondary circulation. The grid Reynolds number, defined as (Thompson and Turner 1975)

$$\mathrm{Re}_G = 0.5 a f_G S^{1.5} M^{0.5} / v \qquad (1)$$

(v is the kinematic viscosity, f_G is the grid oscillation frequency, S is the grid stroke, i.e., twice the oscillation

amplitude, M is the square mesh size while $a \approx 0.1$ is a coefficient), varies in the range 3.3–23.7.

The grid is bound to a stainless steel support frame, connected to a vertical piston rod driven by a motor. Four metal static rods guide the grid and its support movement, limiting the torsional and transverse oscillations. The frame and the piston rod are coupled with a joint able to transmit axial forces, but not moments or lateral forces, so that small assembly and/or alignment errors do not affect the system's behavior or introduce vibration during the grid motion.
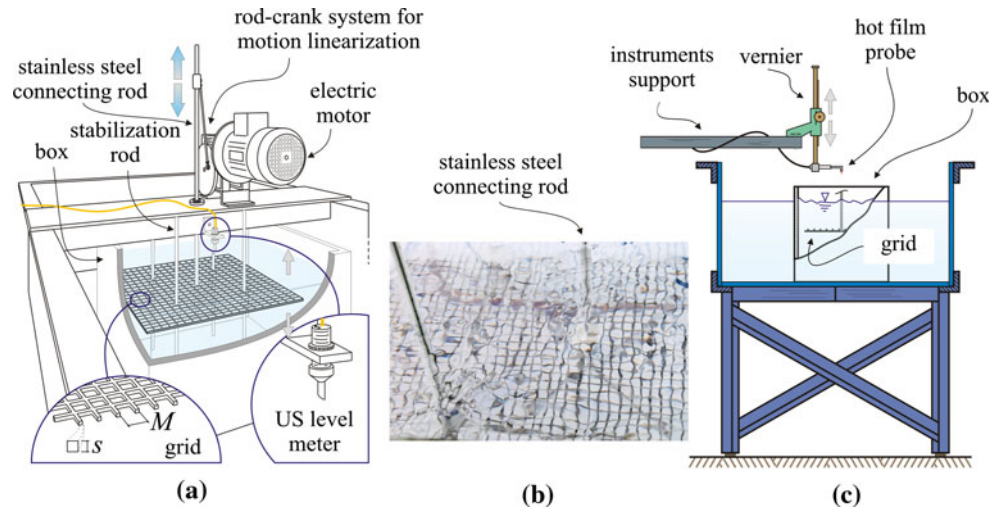
Adjustments of the motor speed and the crank length on the motor flywheel assembly allow a range of grid frequencies between 0.3 and 3.3 Hz and of strokes between 30 and 150 mm. Higher frequencies of the grid were tested and then avoided due to resonance phenomena in the tank. An external support is installed for the hot-film probe, in order to bypass the mechanical vibration of the box.

2.2 Water level and velocity measurements

The velocity measurements were performed using a cone hot-film anemometer (TSI 1231 W) controlled by a TSI analog bridge instrument. The measurement volume of the quartz-coated platinum probe is about the size of the sensing element, a cone 0.5 mm height with a base diameter of 0.25 mm. The axis of the cone probe is aligned to the velocity component to be measured. The probe can be positioned within an accuracy of 0.1 mm and measurements are possible no less than 1 mm beneath the still water level. Effort was made to obtain stable and repeatable measurements. Water was deionized, deaerated, and filtered during hot-film calibration and at the beginning of each test. Calibration was performed at the beginning and at the end of each test by using a towing system controlled by PC to move the probe in still water at known speeds. The overall accuracy is equal to 2 % of the actual reading. The frequency response of the system is slightly greater than 5 kHz. Data acquisition is through a fast speed data acquisition board (DAQ) at a data rate of 10 kHz, with the input signal filtered by an analog low-pass filter with a cut-off frequency at 5 kHz to avoid aliasing. A complete description of the experimental set-up and of anemometer calibration is in Chiapponi (2010).

An important parameter is the duration of the acquisition, which was chosen by observing the time evolution of the average and standard deviation of measured signal at the same point and in the same condition. After ≈ 150 s, these two values are stable; hence, the minimum duration of data acquisition is set equal to 150 s. The number of cycles for each acquisition is varying from 270 to 500. For a single point of measurements at $z = 5$ mm and for Test 2a, five runs in identical conditions roughly confirmed the

Fig. 1 Layout of the experimental apparatus. On the left **a** you can observe the electro-mechanical device that allows the grid movement, the geometry of the grid and the level transducer; **b** a picture from the top during grid motion; **c** the independent support for the anemometer probe (and its handling system)

variability of both the mean velocity and the turbulence given by McKenna and McGillis (2004) since a maximum difference of, respectively, 18 % and of 13 % was found.

Free surface elevations were measured using an ultrasonic sensor (Turck Banner Q45UR, 2005) based on the flight-time of a carrier wave at 10 MHz, with temperature compensation and a sensing range of 50–250 mm (the distance between the target and the emitter/receiver). The response time was fixed at 10 ms and the overall accuracy is equal to ±0.3 mm. The generated sonic field is conical and divergent, so the measurement surface area varies depending on the distance between the sensor and target. To minimize this effect, a focuser was installed to obtain a circular area of around 10 mm diameter at the distance of measurements. Further details on the accuracy and the performances of this ultrasonic sensor are given in Longo (2010). Also for free surface elevation measurements, a variability of the estimators up to 10 % has been checked among the numerous runs (see Table 1) available for each test. In fact for each point of measurement in the vertical, the data of the free surface level measurements were stored and postprocessed.

A limited set of measurements was taken using a 2D Laser Doppler velocimeter (LDV) by TSI Inc. (see Sect 3.2). The laser source is an Innova 70 Series water-cooled Ar-Ion laser, which can reach a maximum power of 5 W and works with two pairs of laser beams with different wavelengths (green, $\lambda_g = 514.5$ nm and blue, $\lambda_b = 488.0$ nm); each pair defines a plane, and the two planes are perpendicular to each other. The TSI optical modular system has a two-component fiber optics transmitting/receiving probe, which also collects the scattered light, sending it to the elaboration system, as the system works in backward scatter mode. The focus length of the probe lens is 363 mm, and the beam spacing is 50 mm. The half-angle between the incident beams is 3.96°. The measurement volume is defined by the intersection of the four laser beams and has the shape of a prolate ellipsoid whose dimensions are ∼0.08 mm × 0.08 mm × 1.25 mm.

2.3 Experimental procedure and test program

The test conditions can be adjusted by changing the following parameters: (1) the frequency of the grid oscillation f_G ranging 0.3–3 Hz, (2) the stroke S ranging 30–150 mm, (3) the water depth above the maximum level of the grid, $R,$ ranging 50–150 mm. Figure 2 shows a reference scheme describing all the variables. Velocity was measured at several points along the vertical shown in Fig. 2, starting immediately beneath the free surface and moving toward the grid, with an initial spacing of 1 mm and a larger spacing of 2, 5 and 10 mm further from the free surface. It is well documented that the flow field in a grid-stirred tank showed a strong sensitivity to the initial condition, with different flow patterns developing in the tank in a random sequence. To be consistent, each vertical profile was acquired by moving the probe in the vertical direction without stopping the grid oscillation. Table 1 shows the main parameters of all tests. In Sect 3.2, we will show the process of removing the macrovortices from the flow field.

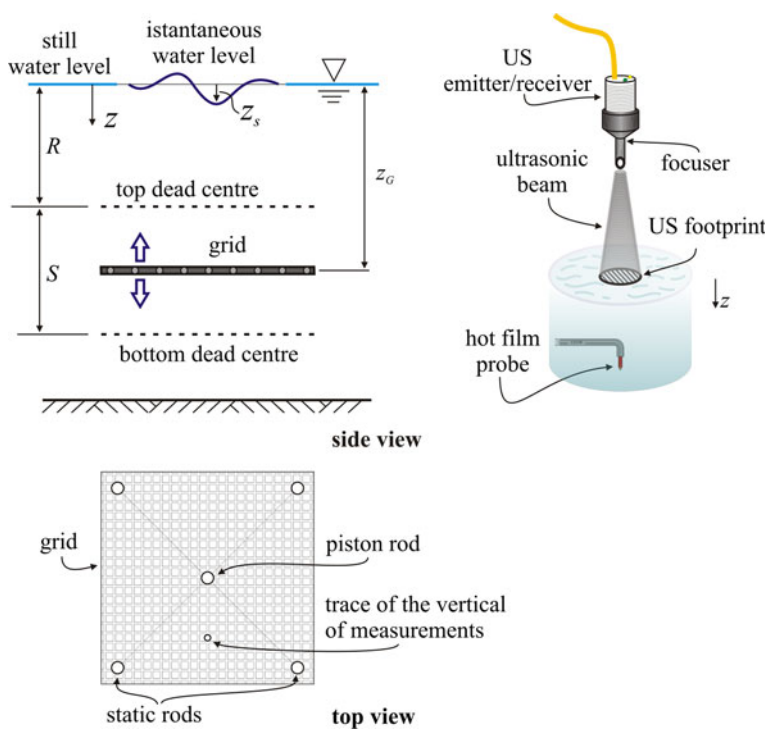## 3 Results and discussion

3.1 Water level statistics

Surface elevation measurements were statistically processed in the time domain using up-crossing analysis to

Table 1 Grid conditions for the experiments

Test (#)	f_G (Hz)	S (mm)	z_G (mm)	R (mm)	Re_G (−)	Re_L (−)	Points of measurement No.
1a	3.29	60	100	70	5.9	67	21
1b	1.83	60	125	95	3.3	50	21
1c	3.30	60	125	95	5.9	63	25
2a	3.28	90	115	70	13.3	91	22
2b	1.88	90	140	95	7.6	69	21
2c	3.30	90	140	95	13.3	86	16
3a	3.25	120	130	70	23.4	112	23
3b	1.88	120	155	95	13.5	85	23
3c	3.30	120	155	95	23.8	106	21

f_G is the frequency of the grid, Re_L is a measure of the turbulent timescale ratio estimated from the grid parameters as $Re_L = \sqrt{15 u'_{rmsHT}(2az)/\nu A}$ with $a = 0.1$, $A = 1$ and u'_{rmsHT} is the horizontal velocity fluctuation proposed by Hopfinger and Toly 1976 (see Eq. 9)

Fig. 2 The reference system and the layouts of the probes

extract $H_{1/3}$, $H_{1/10}$, and $H_{1/20}$, as well as the corresponding periods, $T_{1/3}$, $T_{1/10}$, and $T_{1/20}$ (Table 2).

Previous experiments (Longo 2011; Longo et al. 2012a, b) have demonstrated that the appropriate scales for turbulence near a fluctuating interface are H_{rms} and $u_s = \sqrt{(dz_s/dt)^2}$, where u_s is the root mean square value of the free surface vertical velocity and z_s is the instantaneous vertical position of the free surface. For flat surface, other scales may be more suitable (e.g., Longo 2010). The material derivative is approximated by the partial derivative $dz_s/dt \approx \partial z_s/\partial t$. Using these two scales, we can define the following non-dimensional groups:

$$\mathrm{Fr}_s = \frac{u_s}{\sqrt{gH_{rms}}}, \mathrm{Re}_s = \frac{u_s H_{rms}}{\nu}, \mathrm{We}_s = \frac{\rho u_s^2 H_{rms}}{\sigma} \quad (2)$$

where ρ is the mass density, ν is the kinematic viscosity, and σ is the surface tension. The first is the Froude number, which accounts for the relative significance of the kinetic and gravitational energy in the free surface fluctuations. The second is the Reynolds number, which characterizes the viscous effect. The third is the Weber number, which accounts for the relative importance of surface tension with respect to convective inertia. The suffix s indicates that the scales refer to free surface. H_{rms} is related to the magnitude of the interface fluctuation, while u_s represents its speed.

Table 2 Statistics of the surface elevation

Test (#)	Waves (No.)	T_{mean} (s)	$H_{1/3}$ (mm)	$H_{1/10}$ (mm)	$H_{1/20}$ (mm)	H_{max} (mm)	H_{rms} (mm)	u_s (mm/s)	Fr_s (−)	Re_s (−)	We_s (−)
1a	496	0.30	1.7	2.0	2.2	2.6	1.2	9.8	0.090	12	1.93×10^{-4}
1b	272	0.55	2.0	2.1	2.1	2.2	1.9	8.0	0.058	15	3.96×10^{-4}
1c	575	0.31	1.5	1.8	1.9	2.3	1.1	8.7	0.083	9	1.44×10^{-4}
2a	581	0.25	5.3	8.3	10.4	17.5	3.8	38.9	0.203	147	76.9×10^{-4}
2b	280	0.53	3.6	3.7	3.8	3.9	3.4	14.2	0.077	44	22.49×10^{-4}
2c	543	0.33	2.2	2.8	3.1	4.6	1.6	15.2	0.121	25	5.33×10^{-4}
3a	520	0.28	3.0	3.7	4.0	5.4	2.2	20.2	0.139	50	13.39×10^{-4}
3b	281	0.53	5.5	6.0	6.2	7.7	5.0	22.1	0.099	110	75.68×10^{-4}
3c	819	0.22	6.9	14.5	19.6	30.6	5.5	66.6	0.287	367	0.276

$H_{1/3}$ is the average height of the top 1/3 wave heights, T_{mean} is the mean period of the free surface fluctuations, u_s is the scale of velocity near the free surface, Fr_s, Re_s and We_s are defined in Eq. (2)

Table 2 shows some statistical values and the three non-dimensional parameters of all tests performed.

3.2 The effects of the macrovortices on the velocity fluctuations

The presence of flow patterns due to persistent or random macrovortices induces an overestimation of the turbulence intensity, if simply subtracting time average value from the instantaneous velocity. It is a common problem in most experiments on grid turbulence (e.g., Hopfinger and Toly 1976; McKenna and McGillis 2004), so macrovortices need to be identified. While some specific flow patterns can be detected in the frequency domain and can be removed by filtering, the random flow patterns are much more difficult to eliminate. Here, we suggest a technique based on the knowledge on the expected structure of turbulence in the flow field. This approach assumes that the instantaneous velocity can be decomposed in a mean value, a slowly varying velocity and a fluctuation:

$$w(t) = \overline{w} + \widehat{w}(t) \equiv \overline{w} + \tilde{w}(t) + w'(t) \tag{3}$$

where the overbar indicates the mean (time) value, the tilde indicates the slowly varying velocity computed by a moving time average, and $\widehat{w}(t) = \tilde{w}(t) + w'(t)$. This last variable has been introduced since we do not know a priori the correct time to use in the moving time average in order to separate the slowly varying velocity. In order to analyze the specific case of the grid-stirred tank, a limited set of measurements were taken with a 2D LDV at the same point but rotating the optics (see Tonelli et al. 2010). The use of the laser, instead of the hot-film anemometer, is recommended in this case because the geometry of the hot film could interfere with the pattern of turbulence if measurements have to be taken along direction different from the vertical. In addition, Laser Doppler is not invasive at all. As a counterpart, the data rate of the hot-film

anemometer is much larger than the data rate of the LDV. The output gives several values of the autocorrelation $\widehat{V}\widehat{V}$. The adopted LDV has two channels, so each test gives the autocorrelation in two orthogonal directions, that is, $\overline{\widehat{V_1}\widehat{V_1}}$ and $\overline{\widehat{V_2}\widehat{V_2}}$ and the cross-correlation $\overline{\widehat{V_1}\widehat{V_2}}$, which form the Reynolds stress tensor. The Reynolds stress tensor $\mathbf{T}$ is a second-order tensor and will change under a change of coordinate system as $\mathbf{T}' = \mathbf{A}^T \cdot \mathbf{T} \cdot \mathbf{A}$, with $\mathbf{A}$ being the transformation matrix between the two systems, resulting in $T'_{ij} = A_{pi}A_{qj}T_{pq}$. Being a symmetric tensor, its autocorrelation at an angle α with respect to the initial coordinate system is

$$\left(\widehat{V}\widehat{V}\right)_\alpha = \overline{\widehat{u}\widehat{u}}\cos^2\alpha + \overline{\widehat{w}\widehat{w}}\sin^2\alpha - \overline{\widehat{u}\widehat{w}}\sin 2\alpha, \tag{4}$$

where $\widehat{u}$ and $\widehat{w}$ are measured along the initial coordinate system. We need at least three measurements of the autocorrelation at three different angles α_1, α_2, α_3 in order to estimate the tensor. With more than three measurements, we can evaluate the best fit tensor. If we have also measurements of the cross-correlation $\overline{\widehat{V_1}\widehat{V_2}}$, we can include new equations to obtain a more robust estimate.

Using the velocity results from 8 tests at a single point, the best fit values are (see Fig. 3):

$$\overline{\widehat{u}\widehat{u}} = 3.72 \times 10^{-3} \text{ m}^2/\text{s}^2$$
$$\overline{\widehat{w}\widehat{w}} = 3.00 \times 10^{-3} \text{ m}^2/\text{s}^2 \tag{5}$$
$$\overline{\widehat{u}\widehat{w}} = -3.48 \times 10^{-4} \text{ m}^2/\text{s}^2$$

with a ratio $\widehat{w}_{rms}/\widehat{u}_{rms} \approx 0.9$. Several measurements by Hopfinger and Toly (1976) show that, at a distance of $1.5 \times M$ away from the grid, the turbulence is roughly isotropic with a ratio $\widehat{w}_{rms}/\widehat{u}_{rms} \approx 1.1$. The excess of horizontal velocity fluctuations in the present experiments is then attributed to the macrovortices. Note that the aim is to
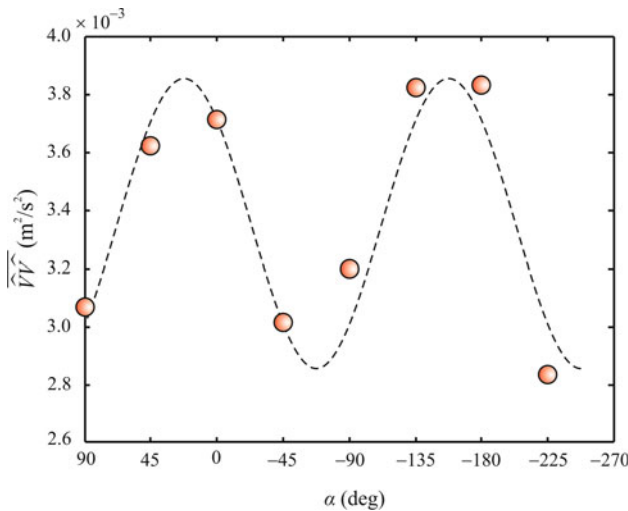
Fig. 3 Fluctuating velocity autocorrelation at different angles. Measurements at $z = 50$ mm. The dashed curve is the best fitting of Eq. (4)

filter the slowly varying velocity contribution in order to obtain $\widehat{w} \equiv w'$ and $\widehat{u} \equiv u'$.

In order to have a measure regarding the degree of anisotropy of turbulence, we can diagonalize the Reynolds stress tensor. The maximum and minimum values of the autocorrelation are computed as

$$
\begin{aligned}
\overline{\widehat{V}\widehat{V}} = {} & \frac{\overline{\widetilde{u}\widetilde{u}} + \overline{\widetilde{w}\widetilde{w}}}{2} \pm \sqrt{\left(\frac{\overline{\widetilde{u}\widetilde{u}} - \overline{\widetilde{w}\widetilde{w}}}{2}\right)^2 + \overline{\widetilde{u}\widetilde{w}}^2} \\
\equiv {} & \frac{\overline{(u'+\widetilde{u})(u'+\widetilde{u})} + \overline{(w'+\widetilde{w})(w'+\widetilde{w})}}{2} \\
& \pm \sqrt{\left(\frac{\overline{(u'+\widetilde{u})(u'+\widetilde{u})} - \overline{(w'+\widetilde{w})(w'+\widetilde{w})}}{2}\right)^2 + \overline{(u'+\widetilde{u})(w'+\widetilde{w})}^2}
\end{aligned}
$$
$$(6)$$

and the angle of their occurrence is

$$
\alpha_p = \frac{1}{2}\tan^{-1}\left(\frac{2\overline{\widetilde{u}\widetilde{w}}}{\overline{\widetilde{u}\widetilde{u}} - \overline{\widetilde{w}\widetilde{w}}}\right)
\tag{7}
$$

The computed values are $\overline{\widehat{V}\widehat{V}}_{\max} = 3.86 \times 10^{-3}$ m^2/s^2, $\overline{\widehat{V}\widehat{V}}_{\min} = 2.86 \times 10^{-3}$ m^2/s^2 and $\alpha_p \approx 23°$. Turbulence structure, thus, is far from isotropic.

Separating the slowly varying component and the fluctuations as shown in Eq. (3) gives results dependent on the average interval t_{ave} adopted to compute the slowly varying component. The dependence is listed in Table 3. The Degree of Anisotropy (DOA) is defined as:

$$
\text{DOA} = \overline{\widehat{V}\widehat{V}}_{\max} \Big/ \overline{\widehat{V}\widehat{V}}_{\min} - 1
\tag{8}
$$

and R^2 is the coefficient of determination of the best fit. If the slowly varying components were zero, the DOA should decrease monotonically for decreasing values of t_{ave}; since

the isotropy is typical of small scales, it is only required that the volume of measurements is small enough to detect these small scales without averaging them. In the present context, the autocorrelation at a given angle (Eq. 4), the angle of occurrence of the maximum/minimum values of the autocorrelation (Eq. 7), and the DOA (Eq. 8) are functions of several variables. For the DOA, we can write in compact form:

$$
\begin{aligned}
\text{DOA} = {} & f\left(\overline{u'u'}, \overline{w'w'}, \overline{u'w'}, \overline{\widetilde{u}\widetilde{u}}, \overline{\widetilde{w}\widetilde{w}}, \overline{\widetilde{u}\widetilde{w}}, \overline{u'\widetilde{u}}, \overline{u'\widetilde{w}}, \overline{\widetilde{u}w'}, \overline{w'\widetilde{w}}\right) \\
\equiv {} & f\left(\overline{\mathbf{u}' \otimes \mathbf{u}'}, \overline{\widetilde{\mathbf{u}} \otimes \widetilde{\mathbf{u}}}, \overline{\mathbf{u}' \otimes \widetilde{\mathbf{u}}}\right)
\end{aligned}
\tag{9}
$$

where $\mathbf{u}' \equiv (u', w')$, $\widetilde{\mathbf{u}} \equiv (\widetilde{u}, \widetilde{w})$, and the symbol $\otimes$ stands for dyadic product. $\overline{\mathbf{u}' \otimes \mathbf{u}'}$ is the Reynolds stress tensor as usually defined, $\overline{\widetilde{\mathbf{u}} \otimes \widetilde{\mathbf{u}}}$ is the Reynolds stress contribution due to the slowly varying velocity components, and $\overline{\mathbf{u}' \otimes \widetilde{\mathbf{u}}}$ is the Reynolds stress contribution due to the interaction between fluctuating terms and slowly varying terms. While for decreasing values of t_{ave} the contribution of $\overline{\widetilde{\mathbf{u}} \otimes \widetilde{\mathbf{u}}}$ tends monotonically to zero (except, perhaps, the non diagonal terms), the contribution of $\overline{\mathbf{u}' \otimes \widetilde{\mathbf{u}}}$ tends to zero but not necessarily in a monotonic fashion. It happens that the mixed correlation terms of this tensor can have a minimum in correspondence of a specific value of t_{ave}. To corroborate this model, we consider that in the present tests, the minimum DOA is almost coincident with the maximum R^2, so the optimal average window is 1.5 s. The measurements necessary to evaluate the optimal time average window were performed for all the different experimental conditions but in a single point at $z = 50$ mm in the position shown in Fig. 2. Similar results are obtained for all tests with slightly different values of the optimal average window. This indicates that the geometry of the system is quite relevant in triggering the macrovortices.

The rotation of the principal axis of the Reynolds stress tensor can also be interpreted by considering the effect of a coherent structure on a field of turbulence. The action of the strain associated with macrovortices or coherent structures is a rotation of the Reynolds stress tensor respect to the strain rate tensor. The misalignment between the two tensors is an indication of the non-local structure of the turbulence field and of the memory effects (see e.g., Champagne et al. 1970; Townsend 1954; Tucker and Reynolds 1968). In general, the turbulent motion appears as 'oriented' by the strain field. If the strain field changes, the axes of the Reynolds stress tensor have a tendency to be reoriented along the axes of the new strain, with a delay related to a relaxation time of the order of the time scale of the imposed strain. Two extreme situations can be conjectured: (1) if the coherent structures could modify the local strain rate without influencing the turbulence field, the Reynolds stress tensor would be forced to rotate in

Table 3 Results of the best fitting model for different values of t_{ave}

t_{ave} (s)	$\overline{\widetilde{u}\,\widetilde{u}}$ (m²/s²)	$\overline{\widetilde{w}\,\widetilde{w}}$ (m²/s²)	$\overline{\widetilde{u}\,\widetilde{w}}$ (m²/s²)	α_p (°)	$\overline{\widehat{V}\,\widehat{V}}_{max}$ (m²/s²)	$\overline{\widehat{V}\,\widehat{V}}_{min}$ (m²/s²)	DOA (%)	R^2 (–)
0	0.00372	0.00300	3.48×10^{-4}	23	0.00386	0.00286	34.9	0.42
0.33	0.00184	0.00196	4.94×10^{-5}	−20	0.00197	0.00182	8.24	0.27
0.50	0.00209	0.00219	4.91×10^{-5}	−23	0.00221	0.00207	6.76	0.17
1.00	0.00253	0.00256	-4.29×10^{-5}	35	0.00259	0.00250	3.60	0.23
1.25	0.00268	0.00267	1.57×10^{-5}	36	0.00269	0.00266	1.13	0.55
1.50	0.00280	0.00277	6.88×10^{-6}	16	0.00280	0.00277	1.08	0.77
1.75	0.00290	0.00286	-1.79×10^{-7}	0	0.00290	0.00286	1.40	0.98
2.00	0.00298	0.00291	-2.12×10^{-5}	−15	0.00298	0.00290	2.76	0.86
2.50	0.00310	0.00299	-4.49×10^{-5}	−20	0.00312	0.00298	4.70	0.78
3.00	0.00320	0.00306	-6.14×10^{-5}	−20	0.00323	0.00304	6.25	0.62
3.50	0.00328	0.00310	-7.84×10^{-5}	−21	0.00331	0.00307	7.82	0.58
4.00	0.00333	0.00315	-9.26×10^{-5}	−23	0.00336	0.00311	8.04	0.59

order to follow the new imposed strain rate; (2) if non-isotropic turbulence could be injected without influencing the strain rate, again the perturbed Reynolds stress tensor would rotate in order to re-align to the undisturbed strain rate tensor. In practice, all coherent structures carry both a distortion strain rate and turbulent stresses; hence, both effects are concurrent in determining the angle shift between the Reynolds and the strain rate tensors.

These results have been applied in the present data analyses to separate the macrovortices from turbulence. As application, in Fig. 4, the vertical velocity profiles of the moving average and turbulent fluctuation velocities are shown for Test 1c. In the present setup and for this test (but not for all tests), the macrovortices induce larger r.m.s. velocities than turbulence, especially near the free surface, where gravity and capillary waves are generated by the turbulence.

In the following, we assume that macrovortices are filtered and only the fluctuating velocity is analyzed and indicated in the figures unless differently stated.

3.3 The vertical velocity fluctuations

Based on the results of Thompson and Turner (1975), Hopfinger and Toly (1976) proposed a relation for the root mean square of the horizontal velocity fluctuation, u'_{rmsHT}:

$$u'_{rmsHT} = 0.25 f_G S^{1.5} M^{0.5} z'^{-1} \qquad (10)$$

where z' is the vertical distance to the middle of the grid oscillation, positive upward. In Fig. 5, the vertical velocity fluctuation profile is shown for different set of experiments and for two preliminary tests, including the theoretical profiles of Hopfinger and Toly (1976) and of Hunt and Graham (1978). The theoretical turbulent velocity profiles
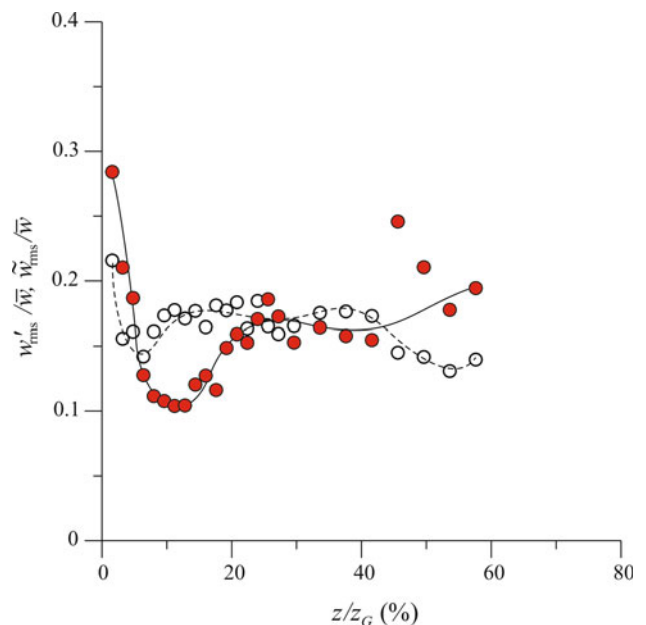

Fig. 4 Vertical velocity fluctuation (*open circle*) and vertical velocity macrovortices fluctuations (*red circle*) profiles. The root mean square values are shown, non-dimensional respect to the mean velocity. Test 1c

by Hunt and Graham is (see also Brumley and Jirka 1987 for further details):

$$w'_{rms} = w'_{rms\infty} \left[\left[1.4 \left(\frac{z}{L_\infty} \right)^{2/3} \right]^{-1.54} \right.$$

$$\left. \cdot \exp\left[-\left(\sqrt{0.558} \frac{z}{L_\infty} \right) \right] + 1 \right]^{-1/3.08} \qquad (11)$$

where $w'_{rms\infty}$ is the far field (far from the surface) root mean square of the fluctuating vertical velocity and L_∞ is the far field longitudinal integral length scale. These values are computed by using Eq. (11) at $z = 0.9 z_G$ (Brumley and
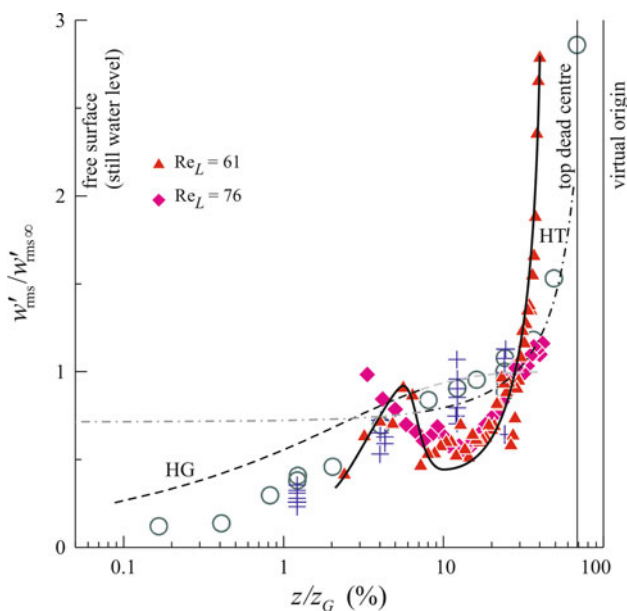
Fig. 5 Normalized vertical velocity fluctuations profile. *Plus* Brumley and Jirka (1987) varied-condition experiment, all sets; *gray circle* Brumley and Jirka (1987) detailed-profile experiments with $Re_L = 74$; *red triangle*, *pink diamond* present experiments. The *dashed line* is the Hopfinger and Toly (1976) relation, the *dashdot line* is the Hunt and Graham (1978) profile, assuming a ratio $w'_{rms}/u'_{rms} = 1.1$; the *bold line* fits the present experiments with $Re_L = 61$
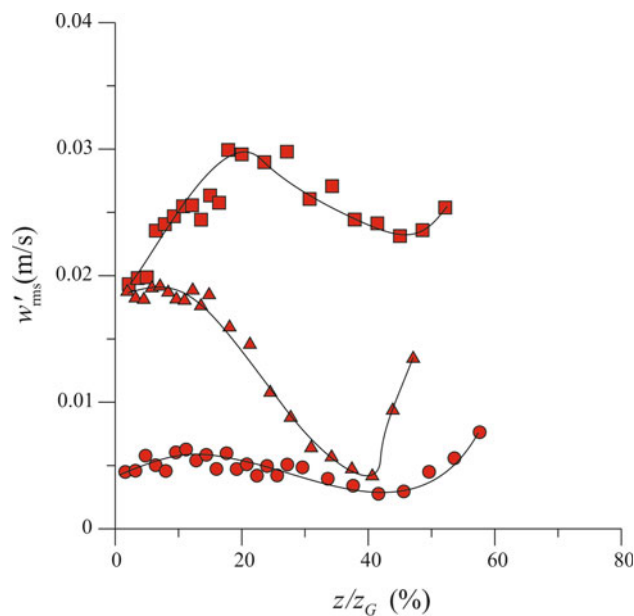

Fig. 6 Vertical velocity fluctuation profiles, r.m.s. value: *red circle* Test 1c, $S = 60$ mm; *red triangle* Test 2c, $S = 90$ mm; *red square* Test 3c, $S = 120$ mm

Fig. 7 Free surface Froude number as function of the free surface Reynolds number. *Filled triangle* $R = 95$ mm, $f_G = 3.3$ Hz; *green circle* $R = 95$ mm, $f_G = 1.8$ Hz; *red square* $R = 70$ mm, $f_G = 3.3$ Hz

Jirka 1987), while it is assumed $L_\infty = 0.1z_G$ (Thompson and Turner 1975). The trend is similar to the theory but a minimum is reached at $z/z_G = 0.10$, then an increment is recorded toward the free surface.

The hypothesis is that a source of turbulence is also present at the free surface due to micro-breaking. Hence, turbulence is generated by the grid and by the free surface and decays far from the sources reaching a minimum. The strength of the source at the free surface is different for different tests; hence, the minimum can be present for some tests and not for other, also considering that the resolution of the measurements near the free surface cannot be sufficient to detect the trend just beneath the free surface.

The effect of increasing stroke is shown in Fig. 6 for tests at a frequency $f_G = 3.3$ Hz. The maximum level of turbulence far from the grid is reached for the maximum stroke ($S = 120$ mm, Test 3c), which looks reliable since larger stroke at given frequency means larger power transferred from the grid to the flow field.

In order to analyze the partition of energy near the free surface, we can consider the dependence of the Froude and of the Reynolds number for varying frequency and amplitude of the stroke; refer to Fig. 7.

For each point of measurements in identical experimental conditions (same stroke, frequency, etc.), we have a statistics of the free surface which is not invariant. Instead
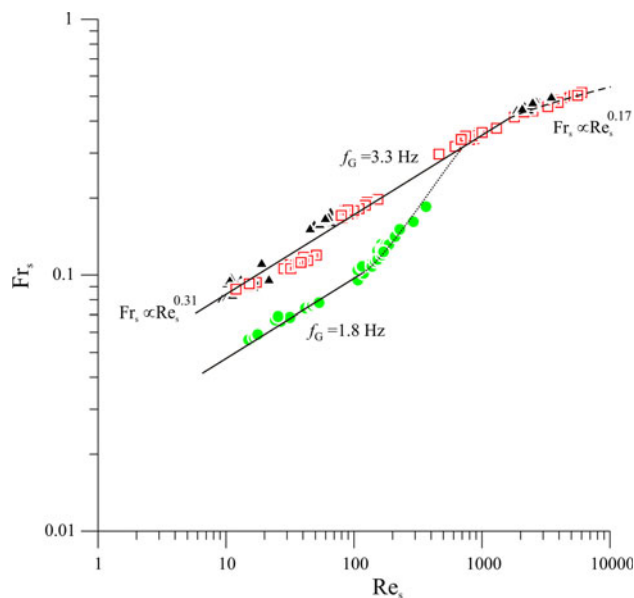
of choosing a single statistics as representative of the test, we included all the validated statistics.

Two separate fitting curves are evident for the two different frequencies of the grid. The fitting curve for the grid frequency $f_G = 3.3$ Hz follows equation $Fr_s = 0.041Re_s^{0.31}$. A similar equation characterizes the lower grid frequency data fitting, with the coefficient equal to 0.25—an almost

identical exponent. The two curves collapse for $Re_s > 1000$; hence, at higher Reynolds number, the turbulence effects on the free surface disturbances loose the memory of the grid movement. For $Re_s > 2000$, there is a bending (dashed curve) due to micro-breaking. Hence, the exponent of the relationship reduces to 0.17 at high Reynolds numbers.

3.4 Spectral distribution of vertical velocity fluctuations

For each acquisition of vertical velocity, the power spectral density was calculated. An example of the computed spectrum is shown in Fig. 8 where filtering for macrovortices has not yet been performed. Some particular frequencies are pointed out. G indicates the grid oscillation frequency and subsequent harmonics are also present. M identifies the frequency of the electric power as converted by the electronic controller. A $-5/3$ spectrum slope is representative of the inertial sub-range in three-dimensional turbulence, which is the case in the bulk region. However, this is not the case when the near-surface region is approached and, more importantly, the emergence of the inertial subrange requires a Reynolds number based on the macroscale, namely $Re_\Lambda = u\Lambda/v$, where u is the macroscale of turbulence, to be larger than 10^5 (or at least larger than 4×10^3 with some weaker hypothesis, see Tennekes and Lumley 1972). Such a high Reynolds number is not achieved in the present experiments, so no inertial subrange is expected. Here, the flow motion in the vertical direction

Fig. 8 Example of vertical velocity power spectrum for the Test 1a and for the point closest to the free surface ($z = 2$ mm); 22 degrees of freedom, frequency resolution 0.153 Hz. The *dashed lines* delimitate the 95 % confidence level band. G grid frequency and subsequent harmonics; M, harmonic frequency of electric engine with the subharmonic N. The spectrum also includes the macrovortices contribution
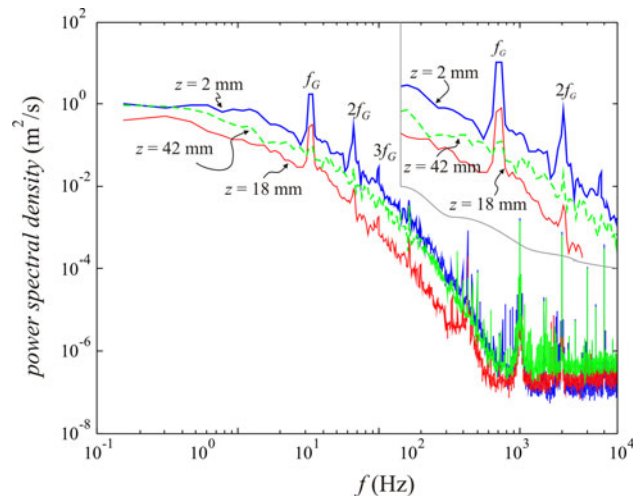

Fig. 9 Comparison of vertical velocity power spectrum for three points in the Test 1a, 22 degrees of freedom, frequency resolution 0.153 Hz. The spectra also include the macrovortices contribution

is restricted and the flow becomes more two-dimensional. The inertial sub-range for two-dimensional turbulence is characterized by a slope of -3 (Batchelor 1969). The -2 slope may be related to the stretching of the turbulent eddies from three dimensions in the bulk to two dimensions as they approach the surface (Herlina and Jirka 2008). A similar behavior is recorded for other level of measurements; refer to Fig. 9. These spectra show that, in this specific test, turbulence energy generally decreases far from the grid then increases again at all frequencies toward the free surface and the spikes at the grid frequencies and its multiples are also enhanced approaching the free surface (see insert in Fig. 9). This last behavior is common to many of our tests and suggests that the grid works well as source of turbulence with a spectrum not biased at specific frequencies (or wave numbers) and the technique adopted to separate macrovortices is also appropriate.

Brumley and Jirka (1987) used a hot-film probe (moving along a circular path) to measure the grid turbulence below the free surface. They obtained a spectrum in the wavenumber domain characterized by a slope of $-5/3$ in the region far from the free surface, and slopes of -3 and -2 near the free surface (-2 at low frequencies). Even though these results are not directly comparable with those of the present work, nevertheless confirm the observed trend in the interface zone.

3.5 Vertical integral and the vertical micro length scale profiles

The vertical integral length scale was estimated from the autocorrelation function in the time domain, by assuming

the frozen turbulence hypothesis by Taylor. Neglecting all terms in the balance of momentum other than fluid acceleration results $\partial/\partial t = -W\partial/\partial z$ where W is the velocity scale, and $w' \ll W$ (w'/W less than ≈ 0.1 and is more likely to be satisfied at a high wave number, see McComb, 1990). This condition is not strictly satisfied in the present flow field but the presence of convective movement, which in general is a flaw in grid-stirred tank, gives an advantage to justify this transformation. Note that the frozen turbulence hypothesis assumes that the small-scale turbulence is simply convected by the large-scale motion and it would be reasonable to choose as convection velocity that associated with the eddies having a scale immediately larger than the scale of turbulence, as happens for the strain rate in the turbulence kinetic energy cascade model. In this respect, the model of Advection Velocity driven by Larger Vortices reported in Longo (2009) is an attempt to follow this approach, but its correct application would require a decomposition in eddies of the whole flow field, not only the separation in macroeddies and fluctuating velocity. This is beyond the aims of the present work.

The time autocorrelation is defined as

$$R_{w'w'}(\tau) \equiv R_{w'w'}(-\tau) = E\{w'(t)w'(t+\tau)\}, \tag{12}$$

where τ is the time lag, and the autocorrelation coefficient is

$$\chi_{w'w'}(\tau) = \frac{R_{w'w'}(\tau)}{w'^2_{\rm rms}}. \tag{13}$$

The integral time scale is

$$\Upsilon = \int_0^\infty \chi_{w'w'}(\tau)\mathrm{d}\tau, \tag{14}$$

and assuming a velocity scale $W = \overline{w}$ the integral length scale is computed as

$$L_w = \Upsilon|\overline{w}|. \tag{15}$$

Figure 10 shows the results for a single test compared with the transverse integral length scale of the experiments by Brumley and Jirka (1987), together with the theoretical relations by Hopfinger and Toly (1976) and by Thompson and Turner (1975). A cube-root distortion of the depth scale has been used for a better view near the free surface. It seems that there is a good match with the theoretical predictions, with a high level near the grid and an almost uniform distribution away from the grid. This length scale is underpredicted by both theoretical profiles near the grid. The present data are not detailed enough near the free surface, but an upward trend is clearly evident.

In order to check the relation between the free surface length scale and the turbulence, the integral length scale is
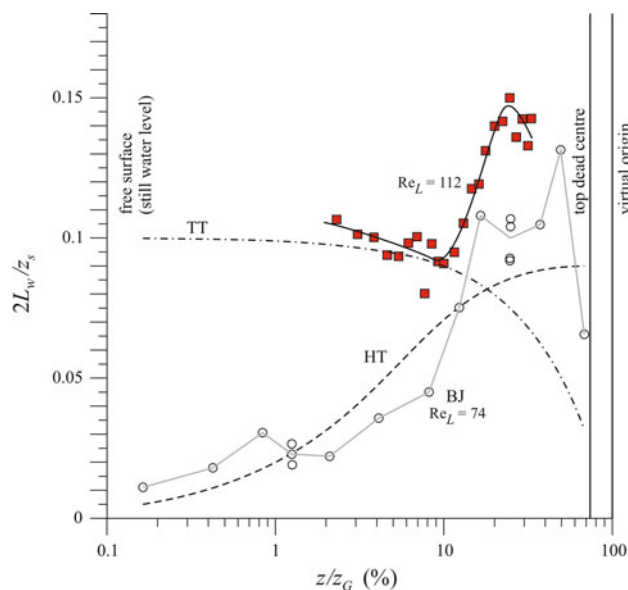

Fig. 10 Normalized vertical length macroscale. *Open circle* Brumley and Jirka (1987) detailed-profile experiments with $\mathrm{Re}_L = 74$; *red square*, present experiments with $\mathrm{Re}_L = 112$. The *dashed line* is the Hopfinger and Toly (1976) relation, the *dashdot line* is the Thompson and Turner (1975) profile, which refers to horizontal velocity fluctuations

non-dimensionalized by $H_{\rm rms}$. Toward the free surface, the integral length scale is generally reduced, and, for large grid strokes, it tends to be equal to $H_{\rm rms}$; refer to Fig. 11a).
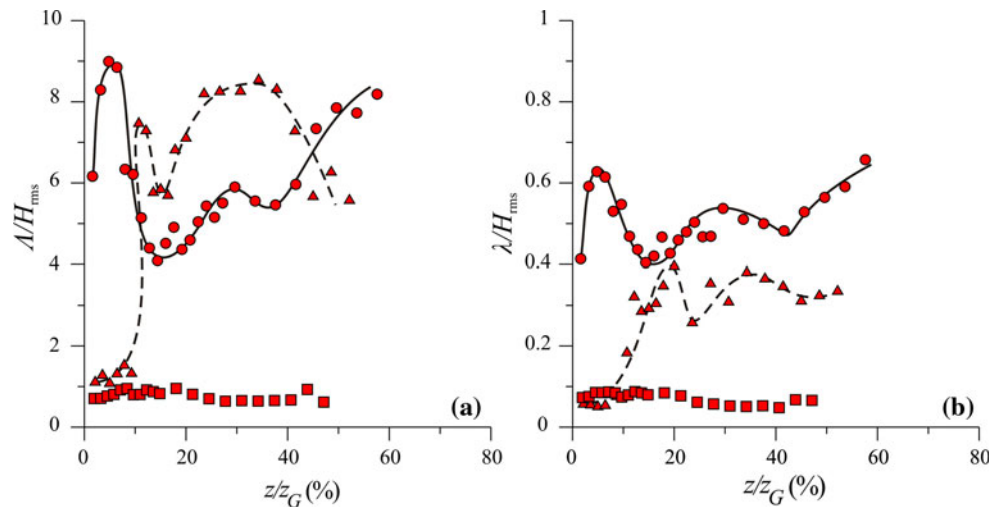
Among the numerous definitions of time microscales, a widely used one is by Taylor, defined as

$$v^2 = -2\left|\frac{\partial^2 R_{w'w'}(\tau)}{\partial\tau^2}\right|_{\tau=0} \equiv \frac{2w'^2_{\rm rms}}{(\partial w'/\partial t)^2}. \tag{16}$$

The correspondent length microscale is computed, according to Taylor's hypothesis of frozen turbulence, as

$$\lambda = v|\overline{w}|. \tag{17}$$

This is not the smallest scale, but it is often assumed as the length scale for the majority of the dissipation to take place. The vertical profiles for some tests are shown in Fig. 11b). Immediately beneath the free surface, the length microscales decrease very fast. Since a reduction in the microscale is linked to higher dissipation rate, we expect that the turbulence energy dissipation profile has a relative peak near the free surface. This profile is thus similar to the dissipation profiles in gravity waves with micro-breaking. For gravity waves in the field, Young and Babanin (2006) show that the vertical profile of dissipation follows z^{-2}. A similar relationship is also reported in Jones and Monismith (2008), who proposed three relationships at different depths. A constant-dissipation layer happens in the range $0 < z < 0.4\,H_s$, where H_s is the significant wave height; a power 2 decay layer (the exponent is -2.2) occurs

Fig. 11 a Vertical length macroscale profiles, same frequency, increasing stroke; **b** vertical length microscale profiles, same frequency, increasing stroke: *red circle* Test 1c, $C = 60$ mm; *red triangle* Test 2c, $C = 90$ mm; *red square* Test 3c, $C = 120$ mm

in the range $0.4\,H_s < z < (d - zt_3)$, where zt_3 is the bed stress log layer; and an increasing trend exists in the bed stress log layer $(d - zt_3) < z < d$. Kudryavtsev et al. (2008) report similar results for the dissipation of turbulent energy. In addition, they show that the turbulent energy production at high wind speed is due to both wave breaking and shearing near the free surface (the role of wave breaking production decreases with the wind), but the wave breaking contribution becomes dominant in the water column up to the depth that the longest breaking waves penetrate. For waves generated in our tank, a moderate shear due to the macrovortices is expected near the free surface; hence, we can expect that both micro-breaking and shearing are responsible for the high dissipation rate near free surface.

The classification of the flow regimes by Brocchini and Peregrine (2001) is based on a velocity scale q, which is related to the Turbulent Kinetic Energy (TKE) by $\kappa = \frac{1}{2}q^2$, and a length scale L, which is related to the dominant surface features on the water side. In the present experiments, we estimated the macroscale computed using the vertical correlation and the vertical fluctuating velocity, from which the TKE can be estimated. The results are shown in Fig. 12, with other data referring to similar analysis for different flow fields. For less energetic tests (small strokes), they fall in the weak turbulence domain, with limited Froude and Weber number. In this condition, wave generation due to turbulence on the liquid side is forecast. Some tests with large strokes fall in the wavy domain, even not far from ballistic domain where droplets separate from the surface. Figure 12 is drawn for static processes and is generally correct except where the dynamic behavior of the free surface becomes dominant, in which situation a third axis representing the time scale of turbulence will be required.

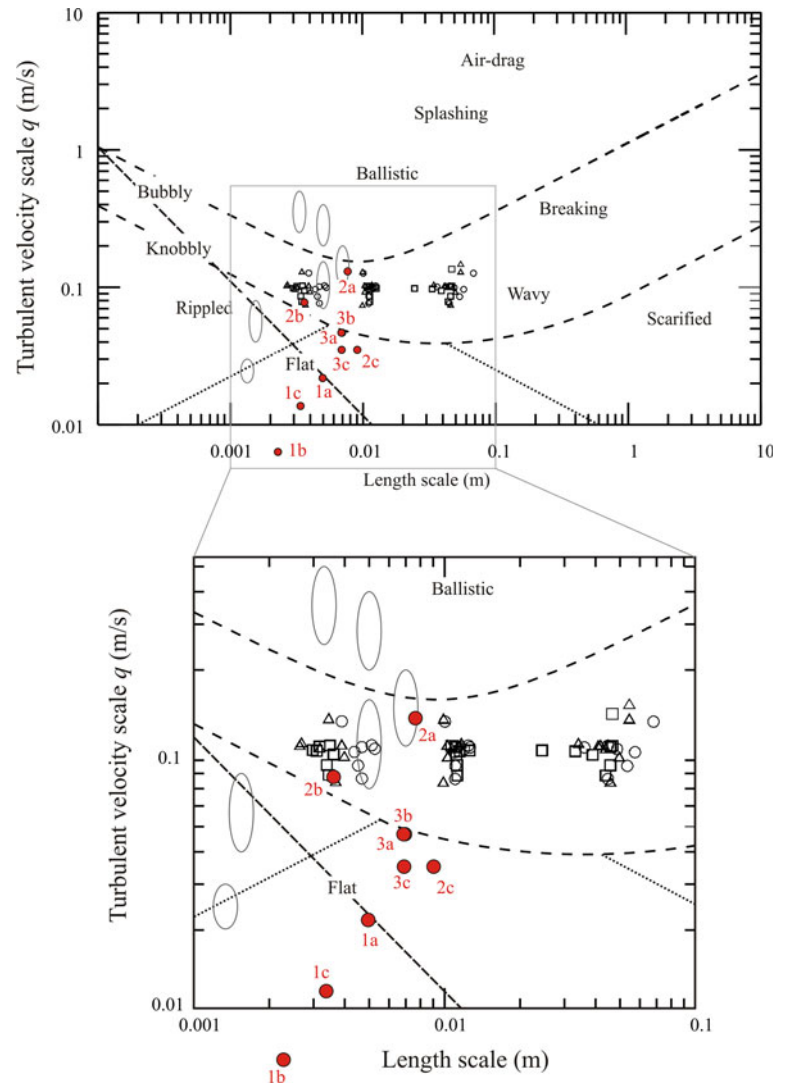### 3.6 The correlation between the free surface and fluid velocity

The coherence between the two variables a and b is defined as

$$\psi = \frac{|P_{ab}|^2}{P_{aa}P_{bb}} \tag{18}$$

where P_{ab} is the power cross-spectral density and P_{aa} and P_{bb} are the power autospectral densities. The coherence ranges between 0 and 1. The analysis of the correlation between the free surface and vertical velocity fluctuations is shown in Fig. 13. Positive values of the phase indicate that the free surface elevations have a delay with respect to the velocity fluctuations. The coherence generally has a maximum value immediately below the mean water level and at frequencies corresponding to the grid frequency or twice this value. This is obviously due to the action of the grid, which transforms part of the energy to pure turbulence, but still induces a coherent motion at free surface. The coherence level decreases with increasing stroke at a given frequency (see Test 1c–2c–3c). The maximum coherence has a value just less than 0.7, and it is larger for smaller H_{rms}.

For significant values of the coherence, we can observe that the phase lag between the free surface fluctuations and the vertical velocity fluctuations is generally negative in the free surface layer, that is, the free surface fluctuations prior to the vertical velocity fluctuations (see Fig. 14); it happens that the phase lag turns into positive values well below the free surface. The super-harmonic of the response occurs because both the crests and the troughs excite the eddies and, hence, the velocity fluctuations. Once again, as reported in Longo (2011), the mechanism of wave generation by turbulence in the water could be as described by

Fig. 12 Diagram of turbulence velocity scale and length scale of dominant surface features (Brocchini and Peregrine 2001). The *bullets* represent the present experiments output; the *ellipses* represent the experiments reported in Longo (2011); the *empty symbols* represent the experiments reported in Longo (2012)

Teixeira and Belcher (2006), with a forcing dominated by turbulent pressure fluctuations. The appearance of microbreakers accelerates the generation of vertical velocity fluctuations.
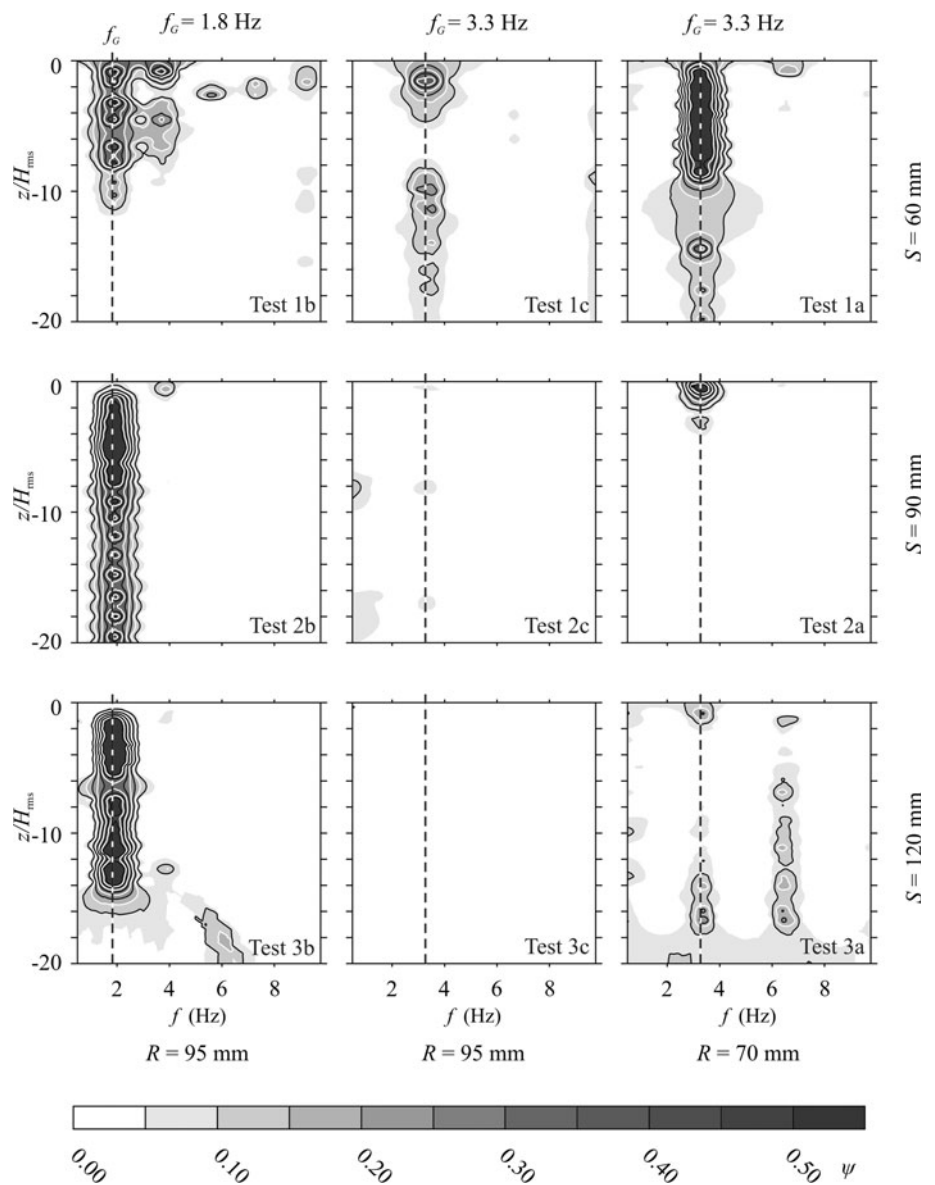
4 Conclusions

A grid-stirred tank has been used to generate nearly isotropic turbulence able to induce free surface distortion. Due to the intrinsic nature of the flow field, some macrovortices arise that could introduce strong errors in turbulence analysis.

- A new method for separating the effects of these macrovortices has been developed based on the expected nearly isotropic structure of turbulence. The general behavior of the tank is coherent with the

behavior of similar tanks adopted in past experimental activity, with velocity fluctuations decaying far from the grid.

- The free surface dynamic has been parametrized through a velocity scale and a length scale; it is expected that the near interface processes are controlled by the Weber number, the Froude number and the Reynolds number related to these two scales. The kinetic energy associated with the free surface fluctuations increases with the Reynolds number with different laws according to the grid frequency but, for Reynolds number larger than ≈ 1000, the curves collapse to a single curve characterized by a lower value of the exponent. Hence, while in general the free surface fluctuations have memory of the source of turbulence through the grid frequency, at higher level of turbulence the process depends solely on the level of turbulence. Also a reduction in the growth

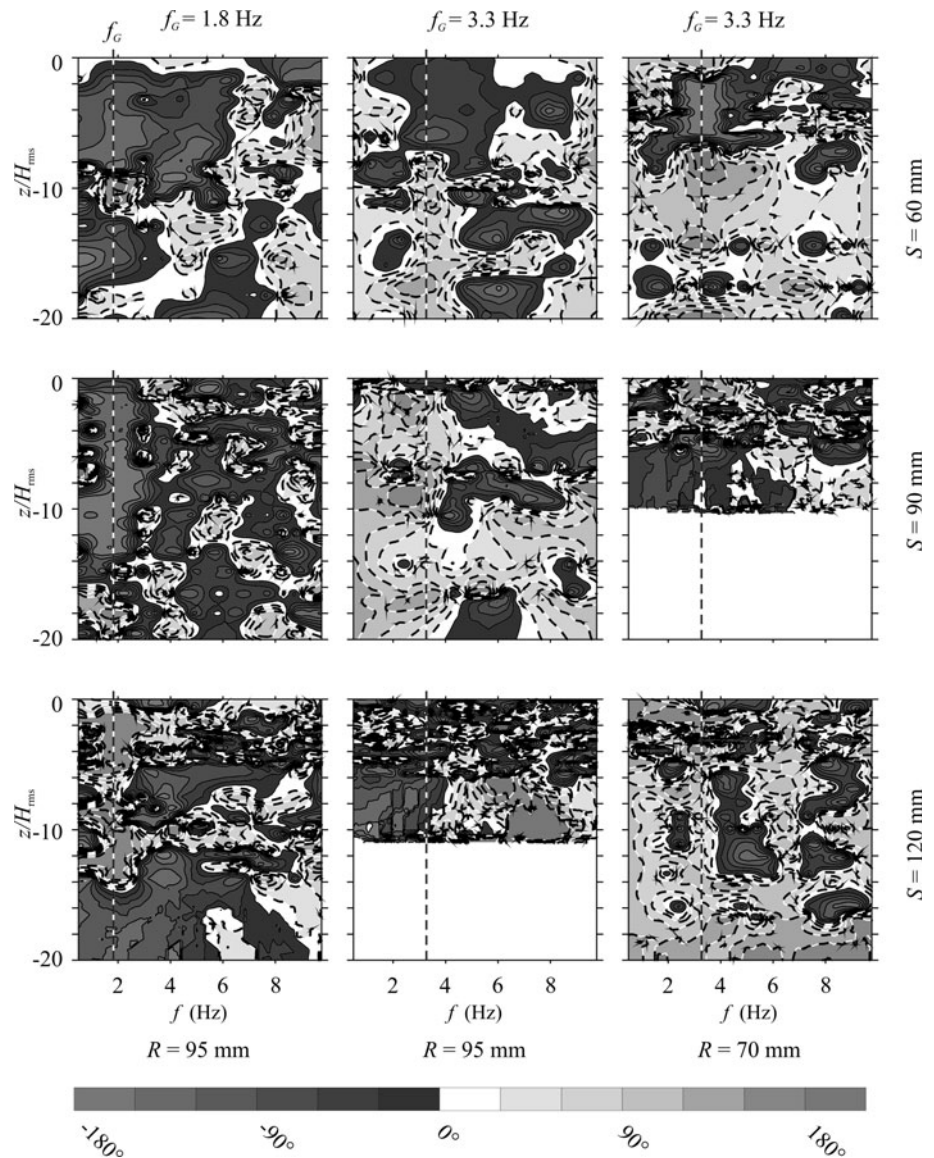**Fig. 13** Coherence map between free surface level and fluctuating vertical velocity

rate of the Froude number is addressed to micro-breaking which also increases the velocity fluctuations immediately beneath the free surface. In these experimental conditions, the inertial sub-range in the vertical velocity fluctuations dynamics is not achieved, since the Reynolds number based on the turbulence scales is below the minimum values of 4×10^3. In fact, except from some spikes, due to the grid action, the estimated spectrum decays with an exponent smaller than -3 (this last value is typical of a two-dimensional turbulence in the inertial subrange).

- The length macroscale, estimated by using the Taylor's frozen turbulence hypothesis, experiences a decay far from the grid then follow reasonably well the profile of

Thompson and Turner (1975). The length microscale has a reduction immediately beneath the free surface: if the estimated length microscales are representative of the dissipation level (the smaller the length microscales, the larger the dissipation rate), an increment of dissipation rate is present in the subsurface layer. This happens also under gravity waves with micro-breaking in the field.

- A classification in the diagram by Brocchini and Peregrine (2001) indicates that most tests fall in the weak turbulence domain, but some tests fall in the wavy domain.

- The analysis of coherence between the vertical velocity fluctuations and the free surface level shows that for significant values of the coherence, the phase

lag is generally negative, that is, the free surface fluctuations are advanced with respect to the vertical velocity fluctuations.

References

Batchelor GK (1969) Computation of the energy spectrum in homogeneous two-dimensional turbulence. Phys Fluids 12(12):233–239

Brocchini M, Peregrine DH (2001) The dynamics of strong turbulence at free surfaces. Part 1. Description. J Fluid Mech 449:225–254

Brumley BH, Jirka GH (1987) Near-surface turbulence in a grid-stirred tank. J Fluid Mech 183:235–263

Champagne FH, Harris VG, Corrsin S (1970) Experiments on nearly homogeneous turbulent shear flow. J Fluid Mech 41(01):81–139

Chiapponi L (2010) Interazione tra superficie libera e turbolenza di forte intensità (Interaction between strong turbulence and fluid interface). PhD Thesis, University of Parma, Italy (in italian)

De Silva IPD, Fernando HJS (1994) Oscillating grids as a source of nearly isotropic turbulence. Phys Fluids 6:2455–2464

Dickinson SC, Long RR (1978) Laboratory study of the growth of a turbulent layer of fluid. Phys Fluids 21:1698–1701

Herlina H, Jirka GH (2008) Experiments on gas transfer at the air–water interface induced by oscillating grid turbulence. J Fluid Mech 594:183–208

Hopfinger EJ, Toly JA (1976) Spatially decaying turbulence and its relation to mixing across density interfaces. J Fluid Mech 78(01):155–175

Hunt JCR, Graham JMR (1978) Free-stream turbulence near plane boundaries. J Fluid Mech 84(02):209–235

Hunt JCR, Stretch DD, Belcher SE (2011) Viscous coupling of shear-free turbulence across nearly flat fluid interfaces. J Fluid Mech 671:96–120

Jones NL, Monismith SG (2008) The influence of whitecapping waves on the vertical structure of turbulence in a shallow estuarine embayment. J Phys Ocean 38:1563–1580

Kudryavtsev V, Shrira V, Dulov V, Malinovsky V (2008) On the vertical structure of wind-driven sea currents. J Phys Ocean 38:2121–2144

Long RR (1978) Theory of turbulence in a homogeneous fluid induced by an oscillating grid. Phys Fluids 21:1887–1888

Longo S (2009) Vorticity and intermittency within the pre-breaking region of spilling breakers. Coast Eng 56:285–296

Longo S (2010) Experiments on turbulence beneath a free surface in a stationary field generated by a Crump weir: free surface characteristics and the relevant scales. Exp Fluids 49:1325–1338

Longo S (2011) Experiments on turbulence beneath a free surface in a stationary field generated by a Crump weir: turbulence structure and correlation with the free surface. Exp Fluids 50:201–215

Longo S (2012) Wind-generated water waves in a wind-tunnel: free surface statistics, wind friction and mean air flow properties. Coast Eng 61:27–41

Longo S, Losada MA (2012) Turbulent structure of air flow over wind-induced gravity waves. Exp Fluids 53:369–390

Longo S, Chiapponi L, Clavero M, Mäkelä T, Liang D (2012a) Study of the turbulence in the air-side and water-side boundary layers in experimental laboratory wind induced surface waves. Coast Eng 69:67–81

Longo S, Liang D, Chiapponi L, Aguilera Jiménez L (2012b) Turbulent flow structure in experimental laboratory wind-generated gravity waves. Coast Eng 64:1–15

McComb WD (1990) The physics of fluid turbulence. Oxford University Press, Oxford

McDougall TJ (1979) Measurements of turbulence in a zero-mean-shear mixed layer. J Fluid Mech 94:409–431

McKenna SP, McGillis WR (2004) Observations of flow repeatability and secondary circulation in an oscillating grid-stirred tank. Phys Fluids 16:3499–3502

Teixeira MAC, Belcher SE (2006) On the initiation of surface waves by turbulent shear flow. Dyn Atmos Oceans 41(1):1–27

Tennekes H, Lumley JL (1972) A first course in turbulence. MIT Press

Thompson SM, Turner JS (1975) Mixing across an interface due to turbulence generated by an oscillating grid. J Fluid Mech 67:349–368

Tonelli M, Longo S, Chiapponi L, Mans C, Losada MA (2010) Grid generated free-surface turbulence laboratory data. Technical Report. University of Udine, University of Parma, Universidad de Granada

Townsend AA (1954) The uniform distortion of homogeneous turbulence. Quart J Mech Appl Math 7(1):104–127

Tucker J, Reynolds AJ (1968) The distortion of turbulence by irrotational plane strain. J Fluid Mech 32:657–673

Young IR, Babanin AV (2006) Spectral distribution of energy dissipation of wind-generated waves due to dominant wave breaking. J Phys Ocean 36:376–394